ADVANCED OPTICAL MATERIALS
www.advopticalmat.de

Third Harmonic Generation Enhanced by Generalized Kerker Condition in All-Dielectric Metasurfaces

*Ai-Yin Liu, Jou-Chun Hsieh, Kuang-I Lin, Snow H. Tseng, and Hui-Hsin Hsiao**

The abundant multipolar resonances in all-dielectric metasurfaces provide a new paradigm to simultaneously induce strong near-field confinement in the interior of a nanocavity as well as to manipulate the far-field scattering property, which is beneficial for the enhancement of nonlinear effects. Here, third-harmonic generation (THG) of all-dielectric silicon metasurfaces that sustain dominant electric dipole (ED), toroidal dipole (TD), and magnetic dipole (MD) moments in near-infrared is numerically and experimentally studied. The effect of the interplay of these resonant modes on THG is investigated, and a pronounced THG enhancement is observed when these modes become spectrally overlapped, corresponding to the generalized Kerker condition. The constructive interference of the total electric dipole (refers to the summation of the ED and TD scattered fields) and MD modes results in the suppression of the backward scattering along with a strong local-field enhancement inside the dielectric resonators. The simulation (experimental) results show a 214-fold (17-fold) THG enhancement in the vicinity of the generalized Kerker condition compared with the signals of the spectrally separated TD and MD resonances. The silicon-based metasurfaces with their simple geometry are facile for large-area fabrication and open new possibilities for the optimization of upconversion processes to achieve efficient nonlinear devices.

1. Introduction

Conventionally, the nonlinear effect of bulk crystals relies on an intensive laser-pumping source under the fulfilment of the phase-matching condition to enhance the intrinsically weak nonlinear response as well as to produce a strong constructive interference effect for the generated radiation. Thanks to the development of nanophotonics, metasurfaces provide a unique platform for strong light–matter interaction by squeezing the external electromagnetic field into regions at a subwavelength scale and thus loosen the phase-matching condition in nonlinear conversion. Recently, the high-index dielectric metasurfaces (DMs) have gained much attention due to their intrinsic low dissipative loss, which is beneficial to achieve high-quality-factor (Q-factor) resonances as well as to sustain large breakdown threshold to the laser power compared with their plasmonic counterparts.[1,2] The electric and magnetic dipole modes, known as Mie resonances, have been widely utilized for more-efficient third-harmonic generation (THG) or second-harmonic generation in many different dielectric nanoresonators made of silicon (Si),[3–6] gallium arsenide (GaAs),[7–10] titanium dioxide (TiO_2),[11] etc. While the Mie resonances provide a strong near-field enhancement inside the subwavelength dielectric resonators that is beneficial for the nonlinear effects, the accompanied radiative loss of these low-order modes intrinsically limits the overall nonlinear conversion efficiency.

In order to minimize the radiative leakage, the interplay between resonant modes has been explored to sustain high Q-factor resonances with narrower linewidths through different coupling mechanisms such as Fano resonances[6,12,13] and quasi-bound states in the continuum (quasi-BICs).[14–19] In addition, the interference of dipolar resonances can be utilized to control the far-field scattering directly based on Kerker effects.[20] As the scattered fields of the electric dipole (ED) and magnetic dipole (MD) modes exhibit an opposite parity, the constructive or destructive interference of these dipolar resonances results in either the suppression of backward scattering or near-zero forward scattering, known as the first and second Kerker conditions, respectively.[21–23] Recently, the employ of multipolar resonances leads to the generalized Kerker effect, which opens a

A.-Y. Liu, S. H. Tseng
Graduate Institute of Photonics and Optoelectronics and Department of Electrical Engineering
National Taiwan University
Taipei 10617, Taiwan
J.-C. Hsieh
Institute of Electro-Optical Engineering
National Taiwan Normal University
Taipei 11677, Taiwan
K.-I Lin
Core Facility Center
National Cheng Kung University
Tainan 70101, Taiwan
H.-H. Hsiao
Department of Engineering Science and Ocean Engineering
National Taiwan University
Taipei 10617, Taiwan
E-mail: hhhsiao@ntu.edu.tw

The ORCID identification number(s) for the author(s) of this article can be found under https://doi.org/10.1002/adom.202300526

DOI: 10.1002/adom.202300526

new paradigm for exotic scattering pattern shaping. For example, the coherent interplay of the ED, MD, electric quadrupole (EQ), magnetic quadrupole (MQ) modes were demonstrated to achieve a transverse scattering pattern that simultaneously suppresses both the forward and backward scattering.[24]

Similar subradiated property along with a strong near-field confinement can also be observed for anapole modes (AMs), but the mechanism of the AM is totally distinct from that of transverse Kerker scattering. The AM is attributed to the destructive interference between the toroidal dipole (TD) and ED moments. The TD moment, known as the vortex distribution of MDs, is originated from currents flowing on the surface of a torus along its meridian.[25–27] Owing to the similar radiation patterns between the TD and ED moments, the destructive interference between these two modes renders a total suppression of the backward and forward scattering field simultaneously. The nonradiative AM with its strong near-field confinement has been utilized for various applications such as THG enhancement[11,28–30] and nanolasers.[31,32] On the contrary, when the ED and TD moments are in phase and interfere constructively, the coherent sum of the ED and TD modes, termed as a total electric dipole (TED), behaves as a super-dipole.[33,34] The suppression of backward scattering has been demonstrated by the interference of the TED and MD modes[33,34] or TED and MQ modes.[24,35]

In this paper, we studied the THG of a series of amorphous Si (*a*-Si) nanopillar arrays embedded in a spin-on-glass (SOG) layer. Upon normal excitation of a plane wave, the *a*-Si nanopillars sustain the ED, TD, and MD resonances in the near-infrared. By varying the diameters of nanopillars, the spectral distance between the TD and MD modes can be effectively tuned, and the effects of each individual resonance and their interplay on THG are investigated. The multipolar decomposition analysis indicates that the ED and TD modes are in-phase at the reflection dip, so that the TED mode behaves as a super-dipole instead of an anapole. The suppression of backward scattering is attributed to the constructive interference of the TED and MD modes. Such Si-based designs are compatible with the state-of-art complementary metal-oxide-semiconductor (CMOS) technology and provide a novel platform to enhance the nonlinear conversion. Meanwhile, the substantial degrees of freedom for substrate materials are beneficial for the on-chip integration.

2. Results and Discussion

Figure 1 schematically illustrates the unit cell of DMs composed of *a*-Si nanopillars with a diameter of *D* and a fixed height (*t*) of 350 nm on a glass substrate. The *a*-Si nanopillars are arranged in a square lattice with a periodicity (*P*) of 850 nm. A SOG layer with thickness of 380 nm is added to fully cover the nanopillars. To investigate the interplay between the resonant modes, a series of samples with four different diameters (*D* = 270, 320, 340, and 360 nm) were designed. Upon the illumination of *x*-polarized light under normal incidence, the simulated transmission spectra (see computational details in the Experimental Section) shown in **Figure 2**a display two resonant dips when *D* is within the range of 320–360 nm. The multipolar decomposition analysis indicates that these two transmission dips are referred to dominant TD and MD resonances, respectively (Figure 2d and Figure S1, Supporting Information). As shown in the top panel

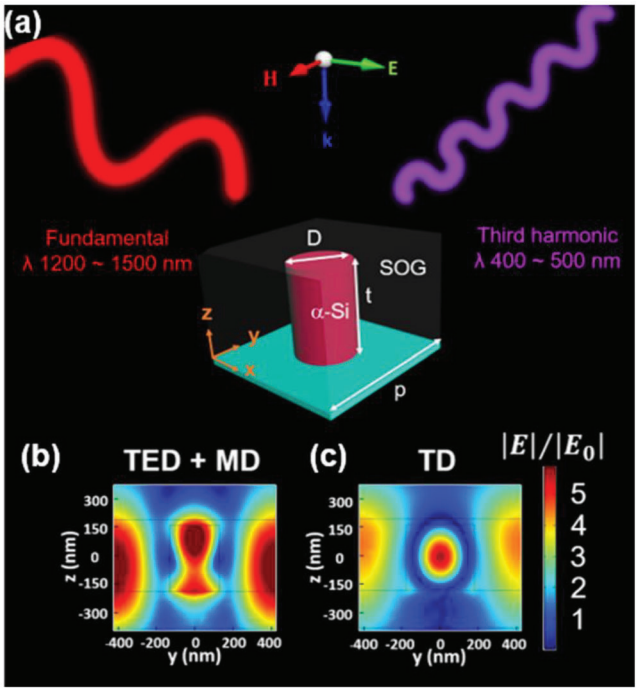

Figure 1. a) Schematic view of nonlinear Si metasurfaces. The electric-field distributions: b) at the reflection dip of *D* = 260 nm and c) at the TD mode of *D* = 360 nm.

of Figure 2e, the near-field distribution of the TD mode reveals a strong enclosed magnetic field profile at the *y*–*z* plane cut. The complete head-to-tail configuration of the MD moments is attributed to the excitation of two out-of-phase MD dipoles pointed at *z* direction (MD_z) combined with two antiparallel MD moments along *y* direction (MD_y) within each individual nanopillar, manifesting the resonant profile of the transverse toroidal mode (see Figure S2, Supporting Information).[36] On the other hand, a strong magnetic field originated from a circular displacement current loop (white arrows) was induced for the MD mode in *x*-*z* plane (Figure 2f). Meanwhile, the corresponding electric-field distributions for both of the TD and MD modes display a strong localized field confined inside the volume of the dielectric nanoresonator (bottom panels of Figure 2e,f).

By decreasing the diameters of nanopillars, both the TD and MD resonances start to blueshift, and the MD mode was found to exhibit a severe spectral shift trend compared with that of TD mode when *D* varies. This leads to the shrinkage of the spectral distance between the TD and MD modes for smaller *D*, and the two transmission dips are merged to a single dip at *D* = 270 nm (Figure 2a). The multipole decomposition analysis shown in Figure S3 (Supporting Information) also validates this trend, and one can find the intensities of the scattering power for both the MD and TD modes increase when they are getting closer in the spectra. The increasing coupling strength between TD and MD modes also leads to the enhancement of the electric-field intensity confined inside the nanocavity for smaller *D* (Figure S4, Supporting Information). Then, a series of samples with different diameters were fabricated through the standard electron beam lithography along with the reactive-ion-etching process (see

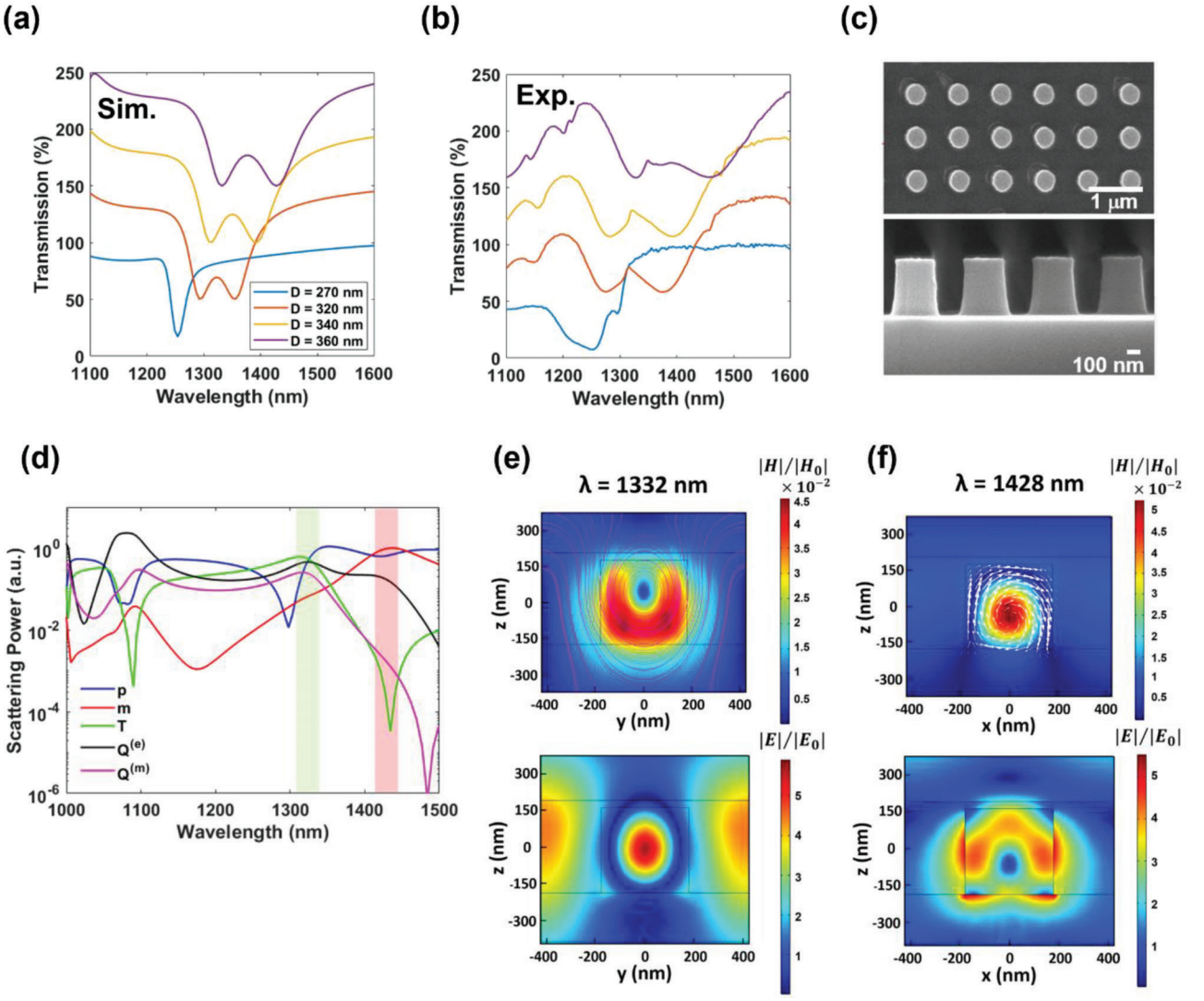

Figure 2. a) Simulated and b) measured transmission spectra for Si nanopillar arrays with four different diameters. c) SEM images of the fabricated sample at the top (upper) and lateral (lower) cross-sectional views. d) The calculated scattering power of each individual electromagnetic multipole moment for $D = 360$ nm. The five strongest multipoles are shown for ***P***: electric dipole, ***m***: magnetic dipole, ***T***: toroidal dipole, ***Qe***: electric quadruple, and ***Qm***: magnetic quadruple. The green and red regions are guides to the eye for the TD and MD resonances, respectively. The magnetic (upper) and electric (lower) field distributions for $D = 360$ nm at: e) the TD resonance and f) the MD resonance. Pink curves in (e) refer to the orientation of the magnetic field, and white arrows in (f) refer to the orientation of displacement currents.

fabrication detail in the Experimental Section). The top and lateral cross-sectional scanning electron microscopy (SEM) images of the fabricated nanopillar arrays prior to the coverage of the SOG layer are displayed in Figure 2c, respectively. The transmission spectra of DMs were then characterized by an in-house–built microscope equipped with a near-infrared spectrometer (see linear optical measurement in the Experimental Section). As shown in Figure 2b, the measured transmission spectra agree well with the simulated results, while the broadening of the resonant linewidths in the measured spectra may refer to the inevitable surface roughness and dimension variation for the fabricated samples.

To perform a comprehensive study of the geometry effect to the evolution of multipolar resonances, **Figure 3**a shows the calculated reflection spectra map as a function of nanopillar diameters. In addition to the shrinking distance between the reflection peaks of the TD and MD modes for smaller D, one can observe a reflection dip occurs at $\lambda = 1225$ nm for $D = 260$ nm (highlighted by a white dashed circle). As aforementioned, both the generalized Kerker effects and the anapole mode can cause a suppression for the backward scattering. To reveal the underlying physics for this reflection dip, we analyzed the phase response of the scattering field contributed from the multipolar moments. Upon the incidence of x-polarized light, the backward radiated electric field to the far-field region in Cartesian coordinates (E^{BW}) can be expressed as[37]

$$E^{\mathrm{BW}} = \frac{ik_0}{2A\varepsilon_0}\left(p_x + ik_0 T_x - \frac{m_y}{c} + \frac{ik_0}{6}Q^{(e)}_{xz} - \frac{ik_0}{2c}Q^{(m)}_{xz}\right) \quad (1)$$

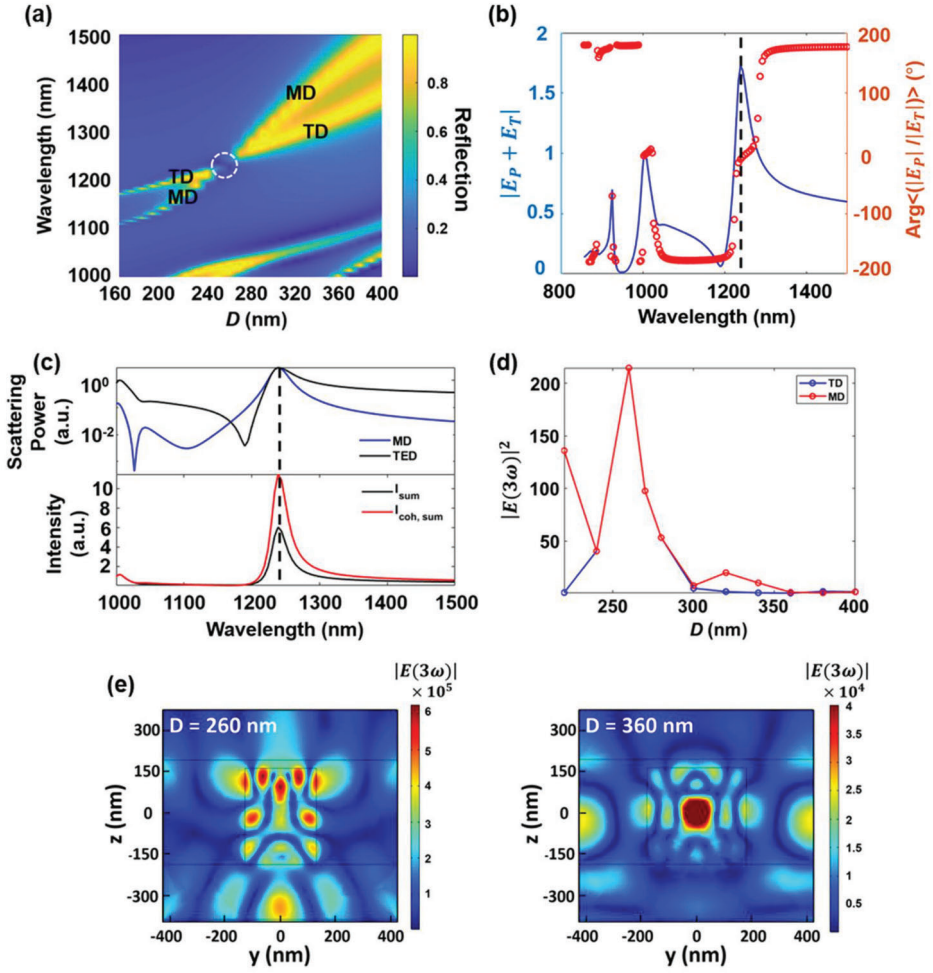

Figure 3. Nonlinear optical properties of Si metasurfaces. a) Simulated reflection spectra of Si metasurfaces as a function of *D*. b) The summation of scattering field (blue curve) and the phase difference (red circles) between the ED and TD moments for $D = 260$ nm. c) Top panel: The scattering power of the TED mode (black curve) and the MD mode (blue curve) for $D = 260$ nm. Bottom panel: The direct power sum (I_{sum}) and the coherent superposition ($I_{coh,sum}$) of TED and MD modes for $D = 260$ nm. The black-dashed line indicates the spectral position of the reflection dip at $\lambda = 1225$ nm. d) The integrated $|E(3\omega)|^2$ as a function of *D* at the TD (blue circles) and MD (red circles) resonances, respectively. e) The cross-sectional (*y*–*z* plane) electric-field distributions at the TH wavelength for $D = 260$ nm (left) and 360 nm (right), respectively, under an input power of 1 W.

where *A* is the area of one metasurface unit cell, and ϵ_0, k_0, and *c* are the permittivity, wavenumber, and light speed in vacuum, respectively. *P*, *m*, *T*, $Q^{(e)}$, and $Q^{(m)}$ refer to the ED, MD, TD, EQ, and MQ moments, respectively. As shown in Figure 3b, the calculated phase difference between the scattering field of the TD and ED modes indicates they are in-phase at the reflection dip (dashed line), corresponding to a maximum of the absolute value for the coherent summation of the TD and ED scattering field, denoted as $|E_{TED}| = |\frac{ik_0 p_x}{2A\epsilon_0} + \frac{-k_0^2 T_x}{2A\epsilon_0}| = |E_p + E_T|$. The constructive interference between ED and TD contributions indicates that TED behaves as a super-dipole at this wavelength, and the suppression of reflection here is not attributed to an AM.

Next, we further took into account the contribution of the MD mode and found both of the scattering power for the TED and MD modes exhibit peaks with an equal magnitude at the reflection dip (upper panel in Figure 3c). In order to examine the interplay of these two moments, the direct power sum (I_{sum}) and coherent superposition ($I_{coh,sum}$) of the TED and MD modes were evaluated as,[34]

$$I_{sum} = |E_{TED}|^2 + |E_{MD}|^2 \quad (2)$$

$$I_{coh,sum} = |E_{TED} + E_{MD}|^2 = |E_{TED}|^2 + |E_{MD}|^2 + 2|E_{TED}||E_{MD}|\cos(\varphi) \quad (3)$$

where E_{TED} and E_{MD} are the scattering field of the TED and MD moments, and φ is the phase difference between the TED and MD moments. As shown in the lower panel of Figure 3c, the larger value of $I_{coh,sum}$ compared with I_{sum} indicates the TED and MD moments interfere constructively. Since the scattering electric field generated by the TED and MD moments displays an opposite parity in the plane of incidence,[35] the constructive interference of the TED and MD modes results in the

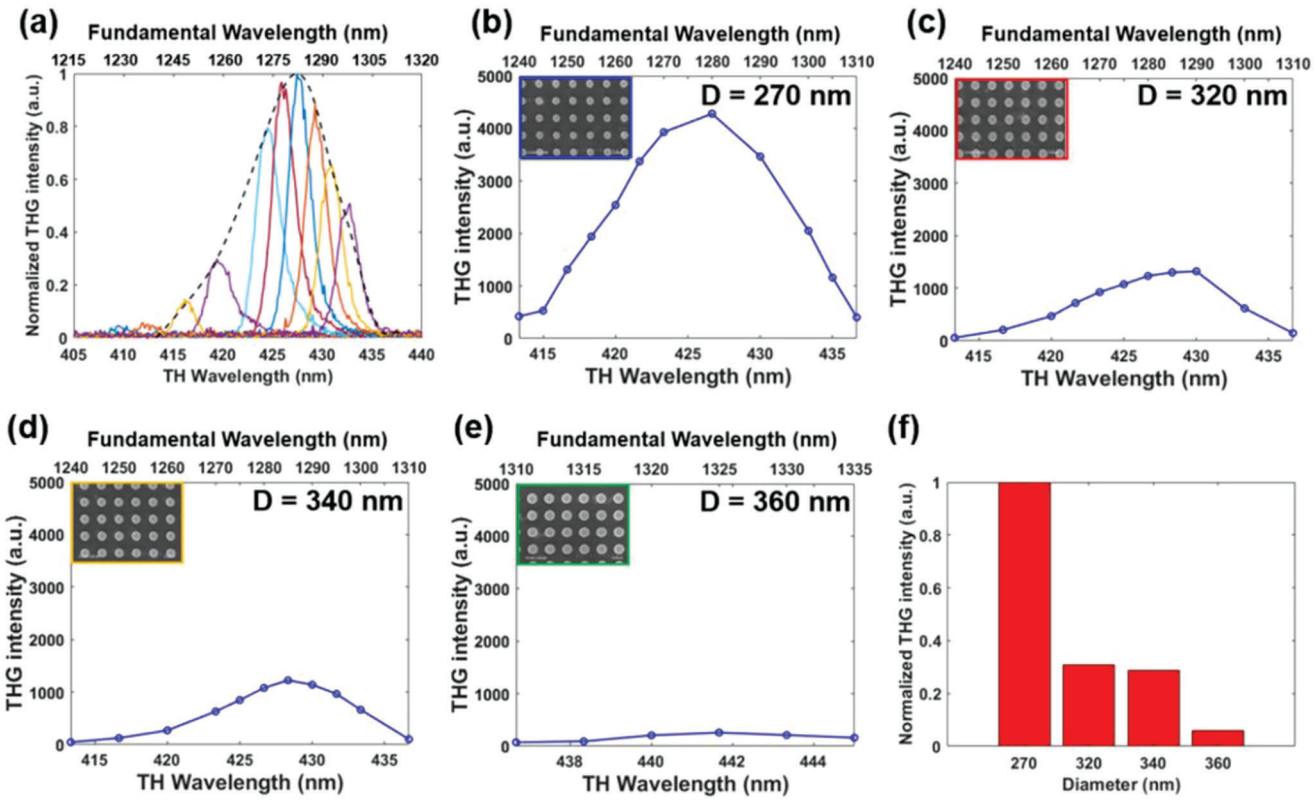

Figure 4. a) Measured THG spectra under different laser wavelength with a fixed initial input power of 100 mW. Color curves refer to the THG signal profile under different fundamental excitation wavelengths, and the black-dashed curve represents the envelope of the color curves. Measured THG spectra for samples with a diameter of: b) 270 nm, c) 320 nm, d) 340 nm, and e) 360 nm. f) Comparison of the peak intensity for the measured THG signal among these samples.

suppression of backward scattering, which is also validated by the calculated far-field radiation pattern (Figure S5, Supporting Information). In addition, one can observe the constructive interference of the TED and MD modes not only causes the suppression of backward scattering but also leads to a remarkable electric-field enhancement (Figure 1b) larger than that of the TD resonance (Figure 1c).

In order to make a theoretical prediction for the effect of the generalized Kerker-type scattering in boosting up the nonlinear conversion, a two-step nonlinear numerical model based on a perturbation theory was implemented to calculate the THG signals.[38] First, the electric field at the fundamental wavelength (FW) was calculated by the linear electrodynamic simulations. Then, the obtained electric field was employed to calculate the nonlinear polarization current as a new source for the nonlinear model through the relation of $P_i(3\omega) = \sum_{j,k,l} \chi^{(3)}_{ijkl}\, E_j(\omega)\, E_k(\omega)\, E_l(\omega)$, where $E(\omega)$ refer to the electric field at the FW, $P(3\omega)$ is the nonlinear polarization at the TH wavelength, and $\chi^{(3)}$ is the third-order susceptibility. The value of $\chi^{(3)}$ is implemented as $2.45 \times 10^{-19}\mathrm{m^2V^{-2}}$ for *a*-Si, and we only considered the dominant elements of $\chi_{xxxx} = \chi_{xxzz} = \chi_{xxyy} = \chi_{yyyy} = \chi_{yyzz} = \chi_{yxxy} = \chi_{zzzz} = \chi_{zyyz} = \chi_{zxxz}$ due to the cubic crystallographic point group of *a*-Si.[39–41] By solving the electrodynamic model at the TH frequency again, we obtained the nonlinear response of DMs. The THG signal was then evaluated by integrating the calculated THG electric field over the whole nanocavity volume (i.e., $I_{\mathrm{THG}} \propto \int |E(3\omega)|^2 dv$). As shown in Figure 3d, the calculated THG intensities (I_{THG}) for samples at the respective TD (blue circles) and MD (red circles) resonances exhibit the same order of magnitude when these two modes are well spectral–separated corresponding to a range of D beyond 300 nm. A remarkable THG enhancement occurs when the TD and MD modes become indistinguishable in the spectra ($D = 270$ nm) and reaches a maximal value when the TED and MD modes are spectrally overlapped and interfere constructively ($D = 260$ nm). The sharp variation of the THG intensity on the nanopillar size renders an enhancement of 98-fold for $D = 270$ nm and 214-fold for $D = 260$ nm, respectively, compared with that of $D = 360$ nm at TD resonance. Such giant enhancement can also be observed from the calculated nonlinear electric-field distributions at the TH wavelength ($|E(3\omega)|$). As shown in Figure 3e, the $|E(3\omega)|$ of $D = 260$ nm exhibits beyond one order of magnitude stronger than that of the TD resonance for $D = 360$ nm.

Next, the THG intensity for a series of *a*-Si nanopillar arrays was measured by an in-house– built multiphoton excitation microscope combined with an optical parametric oscillator (OPO) pumped by a mode-locked Ti:sapphire laser source. The reflected THG intensity was captured through four photomultiplier tubes (see THG measurement in the Experimental Section and Figure S7, (Supporting Information). As shown in **Figure 4**a, the excitation wavelength of the input laser beam was varied to

measure the THG response in the vicinity of the TD resonance for each sample with a sampling wavelength of 5–10 nm. We calibrated the initial input power of the laser beam to retain a value of 100 mW at each fundamental excitation wavelength, so the measured TH signals can be compared directly. As shown from Figures 4b–4e, the spectral positions of the THG peaks redshift for samples with larger diameters in accordance with the spectral variation of the TD resonance. Figure 4f summarizes the measured peak value of the THG intensity for each sample. The THG intensity increases slightly when TD and MD modes are getting closer for samples with D varied from 360 to 320 nm and has a substantial enhancement when these two modes become spectrally indistinguishable for the case of $D = 270$ nm. The measured THG intensity for $D = 270$ nm in the vicinity of the generalized Kerker effect exhibits an 17-fold enhancement compared with the signal of $D = 360$ nm at the TD resonance. The trend of the measured THG intensity among these samples shows good correspondence to our numerical analysis (Figure 3d). The relatively small THG enhancement compared with the numerical prediction may be attributed to the fact that the near-field inside the dielectric cavity has a significant intensity variation at the range when the TED and MD modes become spectral indistinguishable (Figure S4, Supporting Information). Since the spectral distance between these modes is controlled by the nanopillar diameters in our case, a slight detuned diameter of fabricated samples will cause a sharp variation of THG intensity in the vicinity of the generalized Kerker condition, which can also be observed from our numerical prediction for the cases around $D = 260$ nm (Figure 3d). In addition, it is also interesting to compare the THG intensity arisen from the generalized Kerker condition and the anapole state since both of them exhibit the subradiant property along with a near-field enhancement. As shown in Figure S6 (Supporting Information), the calculated magnitude of the electric field at the generalized Kerker condition is much larger than that of the AM. We also measured the THG signal at the AM of $\lambda = 1250$ nm for $D = 360$ nm and found the THG intensity in the vicinity of the generalized Kerker condition for

$D = 270$ nm is 116 times larger than that of the AM for $D = 360$ nm.

Finally, the dependence of the measured output power on the pump power for the metasurfaces was investigated. **Figure 5**a displays the measured THG under different initial excitation power varied from 20 to 250 mW at $\lambda = 1280$ nm for $D = 270$ nm. For the average input powers below 140 mW, the THG power follows the expected trend of a cubic dependence on the FW excitation power with a slope of 3.05 (Figure 5b). For higher pump intensities, the dependence shows a typical saturation behavior, which may arise from the laser-heating effect that causes a small refractive-index change of a-Si resonators and leads to the resonant wavelength shift.[11,28,29] Similar process was also conducted for the sample of $D = 360$ nm and acquires a slope of 3.12. The absolute THG conversion efficiency defined as $\eta_{TH} = P_{TH}/P_{in}$, where P_{TH} is the collected THG emission power and P_{in} is the input pump power, was estimated to be 2.2×10^{-6} at the average pump power of 12 mW for $D = 270$ nm (peak pump intensity of 23.3 GW cm^{-2}). The peak power intensity was calculated based on the temporal pulse width, the repetition rate, and the spot size of the fundamental beam. Since η_{TH} increases quadratically with the pump power,[29] the normalized conversion efficiency defined by $\xi_{TH} = P_{peak-TH}/P^3_{peak-in}$ ($P_{peak-TH}$ is the peak TH power; $P_{peak-in}$ is the peak pump power)[42] was also evaluated under the assumption that the pulse duration time of THG signal is the same as the pump laser and yields a value of 4.05×10^{-12} W^{-2}.

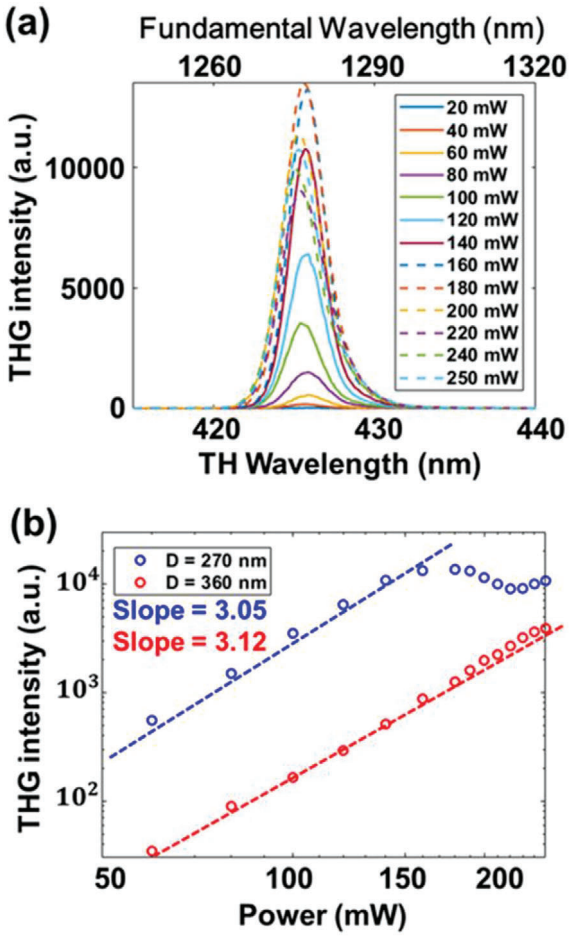

Figure 5. a) Measured THG spectra under different excitation power and b) the log–log plot for $D = 270$ nm (blue circles) and 360 nm (red circles) under a pump wavelength of 1280 and 1325 nm, respectively. The dashed lines are fitting data with a third-order power dependence.

3. Conclusion

We designed an all-dielectric Si metasurface to investigate the interplay of the ED, TD, and MD modes in affecting the THG signals. The spectral distance between the TD and MD modes is tailored by the diameters of nanopillars. When these multipoles are spectral overlapped, the constructive interference of the TED and MD modes leads to a significant suppression of reflection as well as a strong near-field localization inside dielectric nanoresonators. Our simulation (experimental) results show a 214-fold (17-fold) THG enhancement in the vicinity of the generalized Kerker condition compared with the signal of the TD resonance. In addition, the measured THG signal for $D = 270$ nm close to the generalized Kerker condition shows

116 times enhancement than that for $D = 360$ nm at the AM. The measured TH signals were verified and demonstrated a cubic dependence on the excitation power. We believe the results potentially pave the way to establishing a new route toward the optimization of the TH upconversion efficiencies of nonlinear metasurfaces.

4. Experimental Section

Sample Fabrication: The nonlinear DMs were fabricated by first depositing a 350-nm-thick *a*-Si film on a glass substrate by plasma-enhanced chemical vapor deposition (Oxford plasmapro system 100). Then, an electron-beam resist layer (zep520a: Anisole = 1:1) was spin-coated onto the *a*-Si film and followed by the spin-coating of an ESPACER layer to prevent the charging effect during the electron beam lithography (EBL) process. The pattern was defined by an EBL system (ELS-7000) with an acceleration voltage of 100 kV and a beam current of 100 pA. The exposure area of each pattern was 150 × 150 μm^2. After the exposure, the sample was rinsed with deionized water to remove the ESPACER layer and developed in a ZED-N50 solution. Subsequently, a 35-nm-thick chromium film was deposited via electron-beam evaporation. After the lift-off process using *N*,*N*-dimethylacetamide (ZDMAC), the patterns were transferred to chromium disks as hard masks for the following reactive ion-etching process using the reaction gas of CF_4 and O_2 at RF power of 75 W (SAMCO RIE-10NR). The nanopillars were obtained after the removal of chromium disks with a chromium etchant. Finally, a layer of spin-on-glass (SOG) was spin-coated on the fabricated nanopillars.

Numerical Simulation: All simulations were performed using the electromagnetic numerical simulations based on the finite-element method (COMSOL Multiphysics software) in the frequency domain to calculate the linear and nonlinear electromagnetic responses. In the linear model, the refractive index of the glass substrate, SOG, and *a*-Si were set to be 1.5, 1.45, and 3.5, respectively. An *x*-polarized incident light was illuminated normally from the top of the metasurfaces. In addition, a multipole decomposition method was performed for the analysis of the multipolar electromagnetic fields to the far-field scattering by integrating the induced currents over the nanostructures.[43]

$$\vec{p} = \frac{1}{i\omega} \int \vec{J}\, d^3r \tag{4}$$

$$\vec{m} = \frac{1}{2c} \int \vec{r} \times \vec{J}\, d^3r \tag{5}$$

$$\vec{T} = \frac{1}{10c} \int \left[\left(\vec{r} \cdot \vec{J} \right) - 2r^2 \vec{J} \right] d^3r \tag{6}$$

$$\vec{Q}^{(e)}_{\alpha\beta} = \frac{1}{2i\omega} \int \left[r_\alpha J_\beta + r_\beta J_\alpha - \frac{2}{3} \left(\vec{r} \cdot \vec{j} \right) \delta_{\alpha\beta} \right] d^3r \tag{7}$$

$$\vec{Q}^{(m)}_{\alpha\beta} = \frac{1}{3c} \int \left[\left(\vec{r} \times \vec{J} \right)_\alpha r_\beta + \left(\vec{r} \times \vec{J} \right)_\beta r_\alpha \right] d^3r \tag{8}$$

where $\vec{p}$, $\vec{m}$, $\vec{T}$, $\vec{Q}^{(e)}_{\alpha\beta}$, and $\vec{Q}^{(m)}_{\alpha\beta}$ denote as ED, MD, TD, EQ, and MQ moments, respectively. r is the distance vector from the origin (set to be the center of the nanopillar in this case) to arbitrary point positions in Cartesian coordinates. α, β is x, y, z, and c is the speed of light in a vacuum. Under *x*-polarized light illumination, the effective far-field scattering contributed by multipole moments are p_x, m_y, T_x, $Q^{(e)}_{xz}$, and $Q^{(m)}_{yz}$, respectively.

Optical Characterizations—Linear Optical Measurements: The optical property of samples was characterized by an in-house– built microscope (10 × Infinity Corrected objective, numerical aperture NA = 0.25) equipped with a near-infrared spectrometer (Ocean optics, InGaAs detector). A halogen lamp was used as the light source to impinge the sample with a focal spot size of ≈100 μm. A CCD camera was incorporated to the system to capture the location of the fabricated pattern, and the spectra were measured by the spectrometer.

Optical Characterizations—Nonlinear Optical Measurements: The third harmonic generation measurement was performed by using an in-house–built multiphoton excitation microscope (Figure S7, Supporting Information). An OPO combined with a mode-locked Ti:sapphire laser (Coherent Chameleon Vision II) was employed to produce a tunable excitation light source with a wavelength range from 680 to 1600 nm. The laser pulse width was 140–200 fs, and the repetition rate was 80 MHz. The laser pulse was focused onto the sample with a spot size of 2 μm in diameter by using a 20× objective with a numerical aperture of 0.8. The backward TH signal was detected using four photomultiplier tubes along with band-pass filters to acquire signals in the wavelength of interest.

Supporting Information

Supporting Information is available from the Wiley Online Library or from the author.

Acknowledgements

The authors acknowledge financial support from the National Science and Technology Council (NSTC) of Taiwan (grant nos. NSTC 110-2112-M-002-048-MY3 and NSTC 111-2124-M-006-001) and from the National Taiwan University (NTU) (grant nos. NTU-112L7429 and NTU-JP-112L7210). The authors thank Ms. S.-J. Ji for the assistance in SEM experiments of the Instrumentation Center at NTU, which is supported by the NSTC, Taiwan. The authors are also grateful to the Semiconductor Fabrication Lab of the Consortia of Key Technologies and the Nano-Electro-Mechanical-System Research Center, NTU, for their support. The authors gratefully acknowledge Prof. Shih-Hsuan Chia and Prof. Yu-Chien Wen for their useful discussions of nonlinear measurements.

Conflict of Interest

The authors declare no conflict of interest.

Author Contributions

H.-H.H. conceived the idea. A.-Y.L. designed the nanostructures and performed the numerical simulations. A.-Y.L. fabricated the samples and carried out the linear optical measurements. H.-H.H. and A.-Y.L. analyzed the data and wrote the manuscript. K.-I.L. conducted the nonlinear optical measurements. H.-H.H. and S.H.T. supervised the project. All the authors have given approval to the final version of the manuscript.

Data Availability Statement

The data that support the findings of this study are available from the corresponding author upon reasonable request.

Keywords

all-dielectric metasurfaces, generalized Kerker condition, nonlinear optics, third harmonic generation, toroidal dipole

Received: March 3, 2023
Revised: May 23, 2023
Published online: June 27, 2023

[1] I. Staude, J. Schilling, *Nat. Photonics* **2017**, *11*, 274.
[2] A. Arbabi, Y.u Horie, M. Bagheri, A. Faraon, *Nat. Nano* **2015**, *10*, 937.
[3] S. Chen, M. Rahmani, K. F. Li, A. Miroshnichenko, T. Zentgraf, G. Li, D. Neshev, S. Zhang, *ACS Photonics* **2018**, *5*, 1671.
[4] M. K. Kroychuk, A. S. Shorokhov, D. F. Yagudin, D. A. Shilkin, D. A. Smirnova, I. Volkovskaya, M. R. Shcherbakov, G. Shvets, A. A. Fedyanin, *Nano Lett.* **2020**, *20*, 3471.
[5] M. R. Shcherbakov, D. N. Neshev, B. Hopkins, A. S. Shorokhov, I. Staude, E. V. Melik-Gaykazyan, M. Decker, A. A. Ezhov, A. E. Miroshnichenko, I. Brener, A. A. Fedyanin, Y. S. Kivshar, *Nano Lett.* **2014**, *14*, 6488.
[6] Y. Yang, W. Wang, A. Boulesbaa, I. I. Kravchenko, D. P. Briggs, A. Puretzky, D. Geohegan, J. Valentine, *Nano Lett.* **2015**, *15*, 7388.
[7] S. D. Gennaro, C. F. Doiron, N. Karl, P. P. Iyer, D. K. Serkland, M. B. Sinclair, I. Brener, *ACS Photonics* **2022**, *9*, 1026.
[8] S. Liu, M. B. Sinclair, S. Saravi, G. A. Keeler, Y. Yang, J. Reno, G. M. Peake, F. Setzpfandt, I. Staude, T. Pertsch, I. Brener, *Nano Lett.* **2016**, *16*, 5426.
[9] F. J. F. Löchner, A. N. Fedotova, S. Liu, G. A. Keeler, G. M. Peake, S. Saravi, M. R. Shcherbakov, S. Burger, A. A. Fedyanin, I. Brener, T. Pertsch, F. Setzpfandt, I. Staude, *ACS Photonics* **2018**, *5*, 1786.
[10] P. P. Vabishchevich, S. Liu, M. B. Sinclair, G. A. Keeler, G. M. Peake, I. Brener, *ACS Photonics* **2018**, *5*, 1685.
[11] M. Semmlinger, M. Zhang, M. L. Tseng, T. T. Huang, J. Yang, D. P. Tsai, P. Nordlander, N. J. Halas, *Nano Lett.* **2019**, *19*, 8972.
[12] M. F. Limonov, M. V. Rybin, A. N. Poddubny, Y. S. Kivshar, *Nat. Photonics* **2017**, *11*, 543.
[13] G. D. Liu, X. Zhai, L. L. Wang, Q.i Lin, S. X. Xia, X. Luo, C. J. Zhao, *Plasmonics* **2018**, *13*, 15.
[14] N. Muhammad, Y. Chen, C. W. Qiu, G. P. Wang, *Nano Lett.* **2021**, *21*, 967.
[15] S. Xiao, M. Qin, J. Duan, F. Wu, T. Liu, *Phys. Rev. B* **2022**, *105*, 195440.
[16] T.-Y.i Zeng, G. D. Liu, L. L. Wang, Q.i Lin, *Opt. Express* **2021**, *29*, 40177.
[17] J. H. Yang, Z.–T. Huang, D. N. Maksimov, P. S. Pankin, I. V. Timofeev, K.–B. Hong, H. Li, J.–W. Chen, C.–Y. Hsu, Y.–Y. Liu, T.–C. Lu, T.–R. Lin, C.–S. Yang, K.–P. Chen, *Laser Photonics Rev.* **2021**, *15*, 2100118.
[18] L. Xu, K. Zangeneh Kamali, L. Huang, M. Rahmani, A. Smirnov, R. Camacho–Morales, Y. Ma, G. Zhang, M. Woolley, D. Neshev, A. E. Miroshnichenko, *Adv. Sci.* **2019**, *6*, 1802119.
[19] C. Zhou, L. Huang, R. Jin, L. Xu, G. Li, M. Rahmani, X. Chen, W. Lu, A. E. Miroshnichenko, *Laser Photonics Rev.* **2023**, *17*, 2370011.
[20] Y. H. Fu, A. I. Kuznetsov, A. E. Miroshnichenko, Y.e F. Yu, B. Luk'yanchuk, *Nat. Commun.* **2013**, *4*, 1527.
[21] V. E. Babicheva, A. B. Evlyukhin, *Laser Photonics Rev.* **2017**, *11*, 1700132.
[22] W. Liu, Y. S. Kivshar, *Opt. Express* **2018**, *26*, 13085.
[23] I. Staude, A. E. Miroshnichenko, M. Decker, N. T. Fofang, S. Liu, E. Gonzales, J. Dominguez, T. S. Luk, D. N. Neshev, I. Brener, Y. Kivshar, *ACS Nano* **2013**, *7*, 7824.
[24] H. K. Shamkhi, K. V. Baryshnikova, A. Sayanskiy, P. Kapitanova, P. D. Terekhov, P. Belov, A. Karabchevsky, A. B. Evlyukhin, Y. Kivshar, A. S. Shalin, *Phys. Rev. Lett.* **2019**, *122*, 193905.
[25] J. D. Jackson, *Classical Electrodynamics*, Wiley, New York **1999**.
[26] N. Papasimakis, V. A. Fedotov, V. Savinov, T. A. Raybould, N. I. Zheludev, *Nat. Mater.* **2016**, *15*, 263.
[27] C. Zhou, S. Li, M. Fan, X. Wang, Y. Xu, W. Xu, S. Xiao, M. Hu, J. Liu, *Opt. Express* **2020**, *28*, 9690.
[28] G. Grinblat, Y.i Li, M. P. Nielsen, R. F. Oulton, S. A. Maier, *Nano Lett.* **2016**, *16*, 4635.
[29] G. Grinblat, Y.i Li, M. P. Nielsen, R. F. Oulton, S. A. Maier, *ACS Nano* **2017**, *11*, 953.
[30] L. Xu, M. Rahmani, K. Zangeneh Kamali, A. Lamprianidis, L. Ghirardini, J. Sautter, R. Camacho–Morales, H. Chen, M. Parry, I. Staude, G. Zhang, D. Neshev, A. E. Miroshnichenko, *Light Sci. Appl.* **2018**, *7*, 44.
[31] J. S. Totero Gongora, A. E. Miroshnichenko, Y. S. Kivshar, A. Fratalocchi, *Nat. Commun.* **2017**, *8*, 15535.
[32] A. Tripathi, H.a-R. Kim, P. Tonkaev, S. J. Lee, S. V. Makarov, S. S. Kruk, M. V. Rybin, H. G. Park, Y. Kivshar, *Nano Lett.* **2021**, *21*, 6563.
[33] P. D. Terekhov, K. V. Baryshnikova, A. S. Shalin, A. Karabchevsky, A. B. Evlyukhin, *Opt. Lett.* **2017**, *42*, 835.
[34] X. Zhang, J. Li, J. F. Donegan, A. L. Bradley, *Phys. Rev. Mater.* **2020**, *4*, 125202.
[35] X. Zhang, A. L. Bradley, *Phys. Rev. B* **2021**, *103*, 195419.
[36] H. H. Hsiao, A. Y. Liu, *Laser Photonics Rev.* **2022**, *16*, 2100404.
[37] E. E. Radescu, G. Vaman, *Phys. Rev. E* **2002**, *65*, 046609.
[38] J. Sipe, D. Moss, H. Van Driel, *Phys. Rev. B* **1987**, *35*, 1129.
[39] K. Koshelev, Y. Tang, K. Li, D. Y. Choi, G. Li, Y. Kivshar, *ACS Photonics* **2019**, *6*, 1639.
[40] L. Wang, S. Kruk, K. Koshelev, I. Kravchenko, B. Luther-Davies, Y. Kivshar, *Nano Lett.* **2018**, *18*, 3978.
[41] X. L. Yang, S. W.U Xie, *Appl. Opt.* **1995**, *34*, 6130.
[42] G. Yang, S. U. Dev, M. S. Allen, J. W. Allen, H. Harutyunyan, *Nano Lett.* **2022**, *22*, 2001.
[43] V. Savinov, V. A. Fedotov, N. I. Zheludev, *Phys. Rev. B* **2014**, *89*, 205112.